



## Research paper

## Vertically-aligned silicon carbide nanowires as visible-light-driven photocatalysts



Jindui Hong\*, Seyyed Shayan Meysami, Vitaliy Babenko<sup>1</sup>, Chun Huang,  
Santamon Luanwuthi, Jesus Acapulco, Philip Holdway, Patrick S. Grant, Nicole Grobert\*

Department of Materials, University of Oxford, Parks Road, Oxford, OX1 3PH, United Kingdom

## ARTICLE INFO

## Article history:

Received 29 March 2017

Received in revised form 18 June 2017

Accepted 19 June 2017

Available online 21 June 2017

## Keywords:

Aligned silicon carbide nanowires

Large scale

Growth mechanism

Photocatalyst

Visible light

## ABSTRACT

Vertically-aligned crystalline silicon carbide nanowires (VASiCs) (1 mm long and 50–90 nm in diameter) were synthesised in gram scale using SiO<sub>2</sub>-infiltrated vertically-aligned multi-wall carbon nanotubes (VACNTs) and Si powder. *In situ* residual gas analysis was employed to study their formation and revealed CO to be the main by-product during synthesis. The *in situ* studies also showed that the formation of VASiCs begins at 1150 °C with the growth rate reaching a maximum at 1350 °C. A possible growth mechanism was established based on both, *in situ* and *ex situ* characterisation. The VASiCs have an estimated band gap of 2.15 eV, are photocatalytically active, and show strong light absorbance of up to 577 nm. Under UV-vis light (260–800 nm) as grown VASiCs could remove 90% Rhodamine B (RhB) within 30 min. Over period of 4 h under visible light (400–800 nm) more than 95% RhB was removed demonstrating their potential as visible-light-driven photocatalysts.

© 2017 Elsevier B.V. All rights reserved.

## 1. Introduction

Next generation photocatalysis is considered to be one of the feasible strategies addressing today's emerging energy and environmental challenges [1,2]. Tailored nanomaterials with high surface area, abundant surface state, and controlled morphology are essential to meet the requirements necessary for their efficient exploitation in photocatalytic applications [3]. Uniform, well-aligned one-dimensional nanomaterials facilitate electron transfer in the direction of interest and generally improve mass transfer required in energy and environmental applications [4–11]. For example, vertically-aligned carbon nanotubes (VACNTs) and TiO<sub>2</sub> nanotubes showed superior performance in battery applications [4–6], supercapacitors [7,8], solar cells [5,9], and photocatalysis [10,11]. Moreover, silicon carbide (SiC) is one of most promising photocatalysts due to its variable band gap, high electron mobility (400–900 cm<sup>2</sup> V<sup>-1</sup> s<sup>-1</sup>), and high conduction band (up to –1.8 eV) [12–21]. Recently, SiC nanowires with random orientation were developed for the photocatalytic reduction of CO<sub>2</sub> and water [12,13,18,22]. Several methods to synthesise well-aligned

SiC nanowires were reported including multi-wall carbon nanotube (MWCNT) template growth [23], solvothermal methods [24], pyrolysis of silicon precursors [25–27], chemical vapour reaction [28–31], ZnS-assisted vapour-solid reaction [32,33], and carbonisation of aligned silicon arrays, etc. [14,34] Despite these efforts, the production of aligned SiC nanowires in gram scale with tunable diameter and length has not yet been achieved. Yang et al. and Liu et al. have synthesised aligned porous SiC nanowire arrays by the carbonisation of aligned Si nanowires [14,34]. However, due to the confinement of the aligned Si array template, the obtained SiC arrays have fixed diameter (ca. 300 nm) and short length (ca. 20 μm) [14]. The length and diameters of the resultant VASiC nanowires can be tailored using the carbothermic approach by controlling the thickness of VACNTs carpets and the average diameter of the individual CNTs respectively. Pan et al. prepared aligned SiC by reacting aligned CNTs with SiO [23], yet the yield of SiC was limited due to the small area of the CNTs template (15 mm<sup>2</sup> max.) [35]. Recently, we have developed an aerosol-assisted chemical vapour deposition (AACVD) method for the large-scale synthesis (<90 cm<sup>2</sup>, 14 g/h) of aligned MWCNTs carpets with tunable diameter (25–85 nm) and length (0.1–5 mm) [36–38]. These large-area flexible carpets (600 times of that used by Pan et al. [35] in area) of aligned MWCNTs enable the large-scale production of aligned SiC nanowires with tailored structure. Otieno et al. showed that MWCNTs/aluminoborosilicate composites can be generated by infiltrating MWCNTs with a sol-gel method [39]. Here we used a

\* Corresponding authors.

E-mail addresses: [jindui.hong@materials.ox.ac.uk](mailto:jindui.hong@materials.ox.ac.uk) (J. Hong), [nicole.grobert@materials.ox.ac.uk](mailto:nicole.grobert@materials.ox.ac.uk) (N. Grobert).

<sup>1</sup> Present address: Centre of Advanced Photonics and Electronics, University of Cambridge, 9 JJ Thomson Ave, Cambridge CB3 0FA, United Kingdom.

similar sol-gel process but the  $\text{SiO}_2$  was used as Si source for the conversion of MWCNTs to aligned SiC nanowires using a carbothermal reaction.

Previous reports speculated that both, CO and  $\text{CO}_2$ , are formed as by-products influencing the evolution of the SiC nanowires during the conversion reaction [40–42]. For example, Han et al. reported that CO may react with SiO to form SiC nanowires epitaxially while  $\text{CO}_2$  may etch the MWCNTs leading to SiC nanowires with a wider range of diameters [40]. Chiu et al. explained the shorter length of the SiC nanowires compared to the template of CNTs by the  $\text{CO}_2$  etching of the MWCNTs [42]. Despite these past findings and theoretical explanations, the effect of CO and  $\text{CO}_2$  on the structure of VASiCs has not been experimentally investigated yet. Monitoring of these gaseous by-products in real time and *in situ* diagnostics of the production line are essential in order to understand and propose possible growth scenarios for the VASiCs. Herein, we analysed the chemistry of a VASiCs CVD reactor using a quadrupole mass spectrometer to monitor the formation of residual by-product gases. These profiles of gas evolution and furnace temperature were then used to study and establish the growth mechanism of VASiCs.

Studies of aligned SiC nanowires were focused on the synthesis [25,28,29,31–33], structure or their field emission properties [23,24,26,30,34], while their application in photocatalysis is still limited. The aligned structure facilitates the electron transfer, hence improving the solar energy conversion efficiency [43]. Aligned SiC nanowire arrays with enhanced activity in water splitting were reported by Liu et al. [14]. It is well known that the photophysical/electrochemical properties and photocatalytic/photoelectrochemical performance of nanowires are highly dependent on their structure, *i.e.* diameter, length and aspect ratio [44,45]. As such, previously reported methods with fixed SiC nanowire dimensions did not have the flexibility in the applications due to their limited control of their length and diameter. In addition, previous photocatalytic studies of aligned SiC were limited to UV light only. Considering the narrow band gap of SiC nanowires (2.2–2.8 eV) [12,20,42,46], they are expected to be visible-light-responsive, hence being capable of harvesting solar energy more

efficiently than the UV-responsive photocatalysts. In order to verify this, we conducted the photocatalytic studies with VASiCs to degrade dye pollutant (RhB) using both UV-vis light and visible light, demonstrating that the developed VASiCs are efficient and visible-light-driven photocatalysts.

## 2. Experimental

### 2.1. Material synthesis

Individual steps of the preparation of the VASiCs are described below and illustrated in Fig. 1. These include: a) Synthesis of VACNTs, b) infiltration of a  $\text{SiO}_2$ -sol within the VACNTs matrix, c) conversion of the VACNTs into VASiCs, and d) removal of unconverted VACNTs through calcination in air. With a production rate of 14 g/h for VACNTs [38], the scale of production for VASiCs simply depended on the quantity of VACNTs used for the conversion to VASiCs. For example, 0.9 g (3.9 g) VASiCs were collected by loading 1.6 g (6.8 g) of  $\text{SiO}_2$ -VACNTs in a 5 ml (20 ml) alumina boat allowing gram scale production of aligned SiC nanowires. For  $\text{SiO}_2$ -VACNTs, both step c) and d) were omitted and for the semi-converted VASiC/CNTs only step d) was not applied.

#### 2.1.1. Synthesis of VACNTs

VACNTs were prepared using an AACVD setup as described previously [37]. Briefly, an aerosol consisting of 95 wt% ethylbenzene (99%, Sigma–Aldrich) and 5 wt% ferrocene (purified by sublimation from ferrocene 98%, Sigma–Aldrich) was generated by an aerosol generator and introduced into a quartz reactor located in a standard tube furnace. The VACNTs synthesis was carried out at 850 °C in Argon (1000 sccm) for 1 h.

#### 2.1.2. Infiltration of $\text{SiO}_2$ in VACNTs

$\text{SiO}_2$  was infiltrated in VACNTs using a sol-gel method [39]. The sol was prepared by combining tetraethyl orthosilicate (98%, Sigma–Aldrich, TEOS, 2.2 ml) with a mixture of ethanol (absolute, Fisher, 2.2 ml), deionised water (0.5 ml) and nitric acid (70%, Sigma-

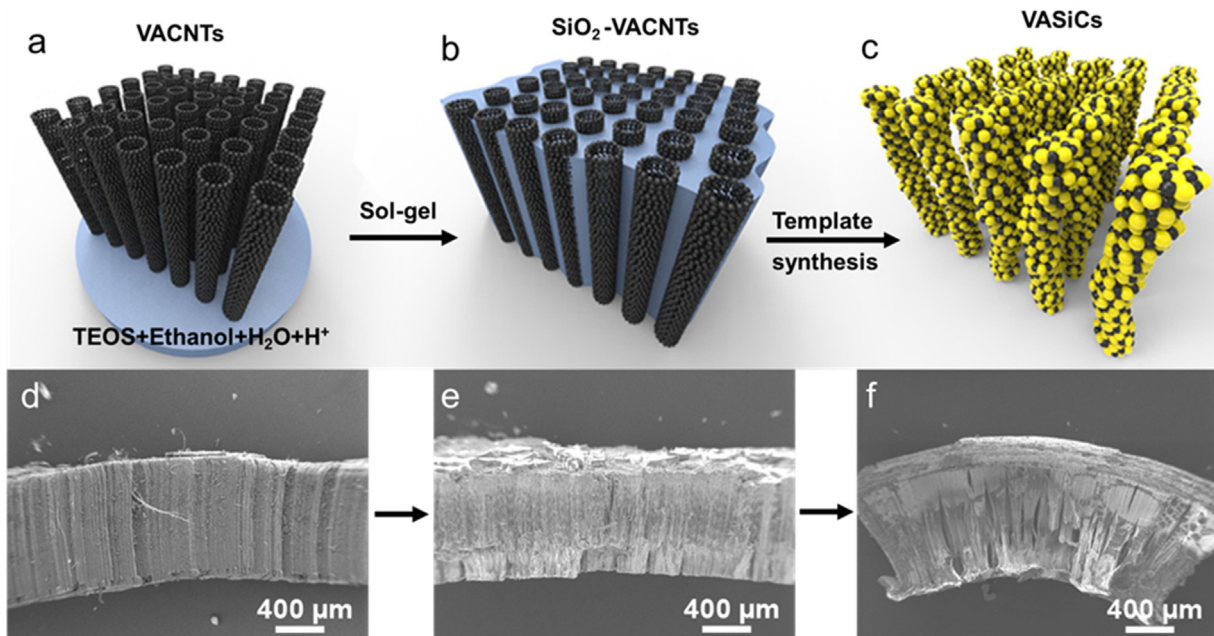


**Fig. 1.** Schematic illustration on the synthesis of VASiCs. Sol-gel: VACNTs placed in the mixture of tetraethyl orthosilicate (TEOS), ethanol, nitric acid ( $\text{H}^+$ ) and deionised water; Template synthesis: heating at 1350 °C in Ar for 3 h then calcination at 900 °C in air for 2 h. Corresponding SEM images of (d) VACNTs, (e)  $\text{SiO}_2$ -VACNTs and (f) VASiCs showing the structure of VACNTs remained intact for all samples except that VASiCs were slightly bent following calcination due to a difference in concentration of the infiltrated sol between the bottom and top end of the VACNT matrix.

Aldrich, 0.5 ml). The as-prepared VACNTs were immersed in the sol up to a height of 1/5th of the VACNTs. The samples were then dried at room temperature for 18 h, calcinated at 350 °C under an air flow (*ca.* 1690 sccm) for 3 h in order to remove any residuals of organic compounds and nitric acid, and finally sintered at 900 °C in Ar (500 sccm).

### 2.1.3. Synthesis of VASiCs

The SiO<sub>2</sub>-infiltrated VACNTs were placed on a layer of Si powder (~325 mesh, 99%, Sigma-Aldrich) in an Alumina boat (5 ml or larger, e.g., 20 ml). The sample was positioned in the centre of a tube furnace heated to 1350 °C in Ar (50 sccm) and the temperature was increased to 1350 °C at a rate of 10 °C min<sup>-1</sup>. The temperature was kept for 3 h. Calcination took place at 900 °C in an air flow (*ca.* 1690 sccm) for 2 h in order to remove any unconverted VACNTs. The as-obtained VASiCs were subjected to NaOH (4 M, 50 ml) at 80 °C for 5 h and then filtrated with deionised water to remove any unreacted SiO<sub>2</sub>.

### 2.1.4. In situ mass spectrometry

Gas residuals were monitored *in situ* using a HPR-20 QIC bench-top quadrupole mass spectrometer gas analysis system (Hiden Analytical) during the formation of the VASiCs. The AACVD setup was connected to the QIC capillary inlet of the mass spectrometer using a T-valve before going to a gas bubbler [47]. Profile scans were carried out in the mass range of 1–50 amu while the multiple ion detection (MID) was performed for the mass to charge ratio (*m/z*) at 28 (N<sub>2</sub> or CO), 32 (O<sub>2</sub>), 36 (<sup>36</sup>Ar), 40 (<sup>40</sup>Ar) and 44 (CO<sub>2</sub>).

## 2.2. Materials characterisation

The size, morphology, orientation, and elemental composition of the VACNTs, SiO<sub>2</sub>-VACNTs, semi-converted VASiC/CNTs, and VASiCs were characterised by scanning electron microscopy (SEM, JEOL-6500F, operated at 5 kV) and transmission electron microscopy (TEM, JEOL-3000F, operated at 300 kV) equipped with

an energy-dispersive X-ray Oxford Instruments Inca spectrometer (EDS). X-ray diffraction (XRD) patterns were obtained using a Bruker D8 Advance ECO diffractometer in a reflection mode at 40 kV and 25 mA using Cu K $\alpha$  radiation ( $\lambda = 1.54057 \text{ \AA}$ ). Thermogravimetric analysis (TGA) was carried out in the temperature range from 40 °C to 900 °C with ramping rate of 10 °C in air (80 sccm) using a Perkin Elmer Pyris 1 thermogravimetric analyser. Raman spectra were collected from a JY Horiba Labram Aramis imaging confocal microscope using a green light laser (532 nm) in the range of 500–3000 cm<sup>-1</sup>. UV-vis diffuse reflectance spectroscopy (UV-vis DRS) was conducted on a Carry 5000 UV-vis-NIR spectrophotometer equipped with a Praying Mantis diffuse reflectance accessory. Mott-Schottky plots at different frequency (1 kHz, 5 kHz and 7 kHz) were recorded on a Reference 600/EIS300 Gamry potentiostat/galvanostat electrochemical workstation. Measurements were performed using a standard three-electrode cell: VASiCs deposited fluoride-tin oxide (FTO) as the working electrode, Pt sheet (1 cm x 2 cm) as the counter electrode, Ag/AgCl as the reference electrode and Na<sub>2</sub>SO<sub>4</sub> aqueous solution (0.2 M) as the electrolyte.

### 2.3. Photocatalytic evaluation

Photocatalytic evaluation was conducted by dispersing VASiCs (10 mg) in 50 ml Rhodamine B (Dye content 97%, Sigma-Aldrich) aqueous solution (10 mg l<sup>-1</sup>). The suspension was stirred in the dark for 2 h in order to reach the adsorption equilibrium prior to the photocatalytic reaction. A 300 W xenon arc lamp (LOT-Oriel Instruments) equipped with a 400 nm long pass filter was used as visible light source. At 30 mins intervals, 1 ml of the suspension was withdrawn using a syringe and filtered through a 0.45 μm PTFE syringe filter to remove the photocatalyst. The filtrate was diluted four times with deionised water. RhB concentration at different time intervals was determined on a Carry 5000 UV-vis-NIR spectrophotometer by measuring the peak intensity at 554 nm. The concentrations of RhB at equilibrium and after photodegradation

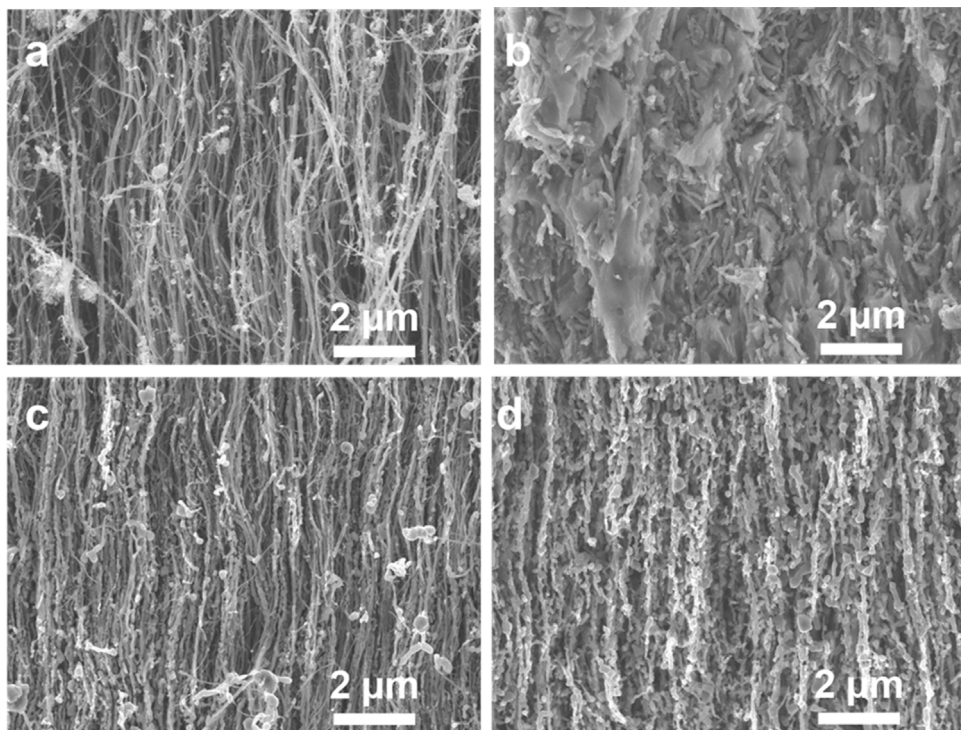


**Fig. 2.** SEM images of (a) VACNTs showing that diameter of CNT is in the range of 20–50 nm, (b) SiO<sub>2</sub>-VACNTs indicating the infiltration of SiO<sub>2</sub>-gel in VACNTs matrix, (c) VASiC/CNTs and (d) pristine VASiCs showing the presence of vertically-aligned nanowires in VASiC/CNTs and VASiCs.

were denoted as  $C_0$  and  $C$ , respectively. Control experiments were performed either in the dark or without VASiCs. To evaluate the recyclability, VASiCs after photoreaction was centrifuged and re-dispersed in fresh RhB solution for another photodegradation.

### 3. Results and discussion

#### 3.1. Structure, composition and sample morphologies

SEM studies revealed that the carpet thickness of the VACNTs was around 1 mm (Fig. 1d) whilst their diameter was in the range of 20–50 nm (Figs. 2 a, 3 a, Fig. S1b).  $\text{SiO}_2$  could be observed on

the surface and between the tubes of the VACNTs suggesting that the VACNTs matrix was indeed infiltrated with  $\text{SiO}_2$  by our sol-gel method (Figs. 1 e, 2 b, 3 b and Fig. S1d). Following the infiltration procedure, the structure of the VACNT remained intact for all samples, the  $\text{SiO}_2$ -VACNTs, semi-converted VASiC/CNTs, and the VASiCs. Although the VASiCs were slightly bent following the calcination process which originated possibly due to a difference in concentration of the infiltrated sol between the bottom and top end of the VACNT matrix. After the conversion, vertically-aligned wires could be observed in both VASiC/CNTs and VASiCs (Fig. 2c and d).

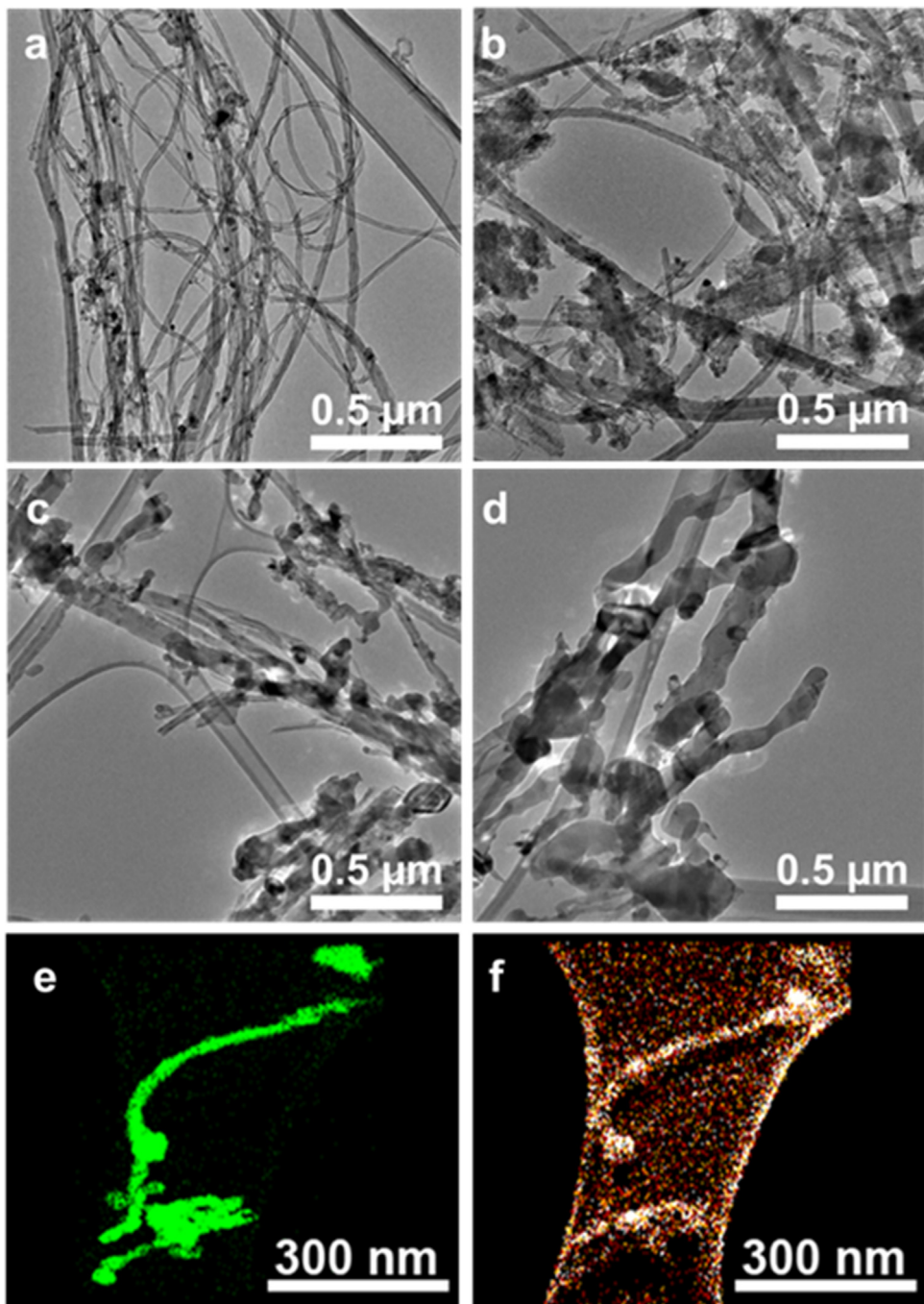


**Fig. 3.** TEM images of (a) VACNTs showing that the diameter is in the range of 20–50 nm, (b)  $\text{SiO}_2$ -VACNTs indicating the infiltration of  $\text{SiO}_2$  in the VACNTs matrix, (c) VASiC/CNTs showing the presence of unconverted VACNTs and (d) VASiCs demonstrating their non-uniform diameter in the range of 50–90 nm. STEM-EDS mapping of VASiCs: (e) Si, (f) C revealing the distribution of elements Si and C in the whole sample while their atomic ratio ( $\text{Si}/\text{C}$ ) is 0.97.

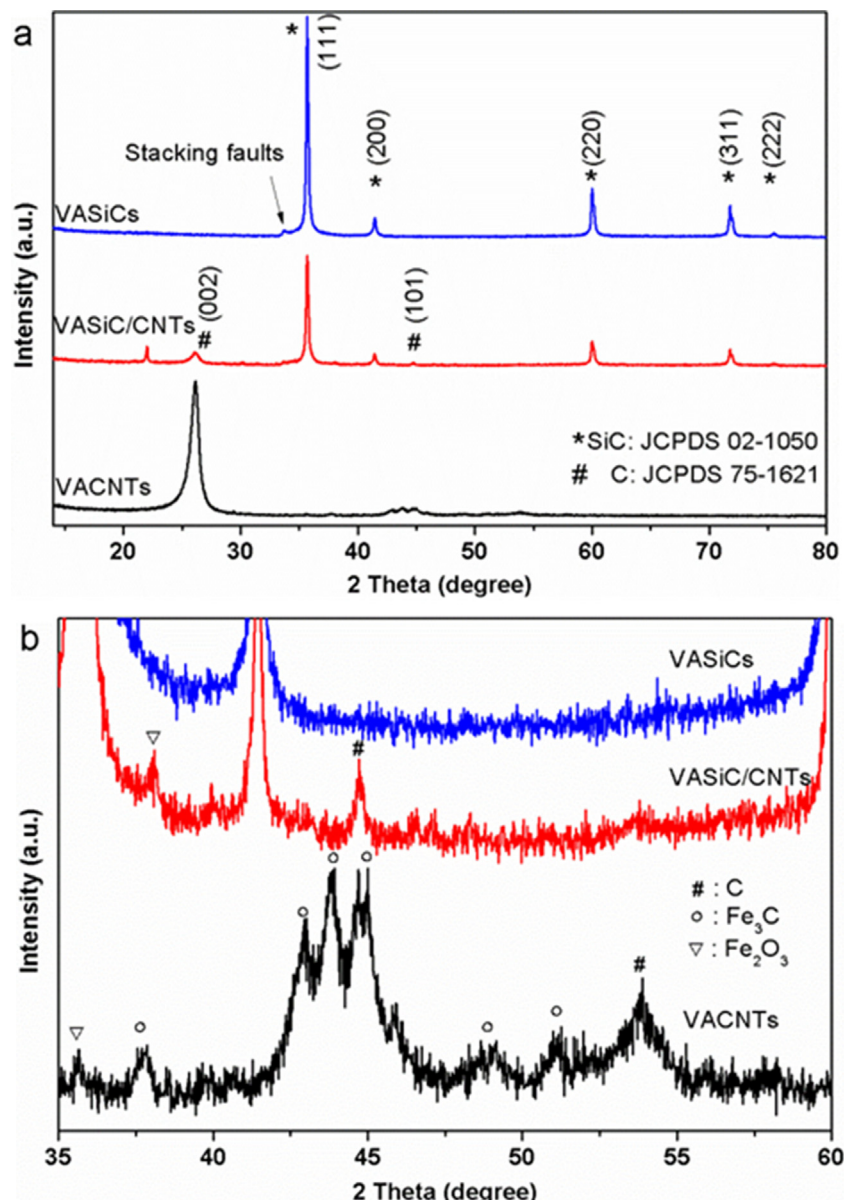


**Fig. 4.** XRD patterns of (a) VACNTs, VASIC/CNTs, and VASICs showing the conversion of VACNTs–VASICs and the cubic structure of VASICs ( $\beta$ -SiC). (b) Close-up view of graph (a) indicating the presence of catalyst residues, iron carbide ( $Fe_3C$ ) and iron oxide ( $Fe_2O_3$ ), in VACNTs, and the removal of  $Fe_3C$  in VASIC/CNTs and the removal of CNT and both catalyst residues in VASICs.

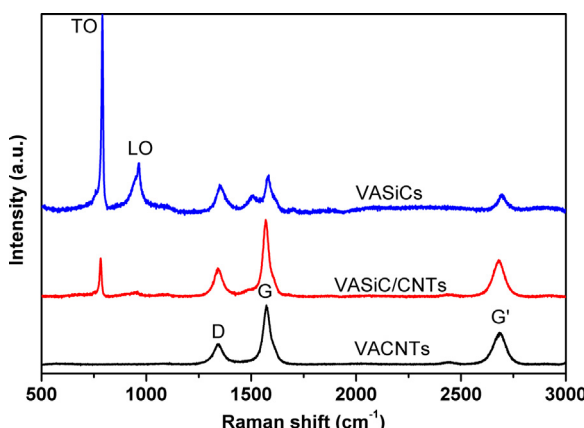


**Fig. 5.** Raman spectra of VACNTs, VASIC/CNTs and VASICs showing typical D band ( $1341\text{ cm}^{-1}$ ), D band ( $1574\text{ cm}^{-1}$ ) and G' band ( $2684\text{ cm}^{-1}$ ) of CNT with low defect intensity ( $I_{D/G} = 0.33$ ), and the transverse optical mode (TO,  $794\text{ cm}^{-1}$ ), longitudinal optical mode (LO,  $967\text{ cm}^{-1}$ ) of SiC.

TEM investigations revealed the presence of some CNT in VASIC/CNTs that did not undergo the conversion process (Figs. 3c and Fig. S2g), which was also confirmed by the EDS mapping of the long nanotubes (Fig. S3). These studies also showed that, on average, the resulting VASICs nanowires (50–90 nm) were ca. 0–40 nm thicker than the ‘left-over’ CNTs and their diameter was not as uniform. Such diameter variation within a SiC nanowire was also reported previously [48–51] and was attributed to the local temperature gradient and gaseous reactant concentration along the CNT [48,51]. The  $d$  spacing of  $2.54\text{ \AA}$  (Fig. S2m) can be assigned to the (111) lattice plane of cubic SiC. STEM-EDS analysis demonstrated that the Si/C atomic ratios in VASIC/CNTs and VASICs were 0.49 and 0.97 respectively, confirming the partial conversion of CNT and the trace of CNT residue in the VASICs sample.

XRD studies of VACNTs revealed peaks at  $26.1^\circ$ ,  $44.6^\circ$  and  $53.9^\circ$  which correspond to the (002), (101) and (004) lattice planes of CNT (JCPDS #75-1621) (Fig. 4a, b). Catalyst residues of iron carbides ( $Fe_3C$ ) and iron oxides ( $Fe_2O_3$ ) were also present in the CNT samples (Fig. 4b) [52,53]. After the template synthesis, SiC patterns

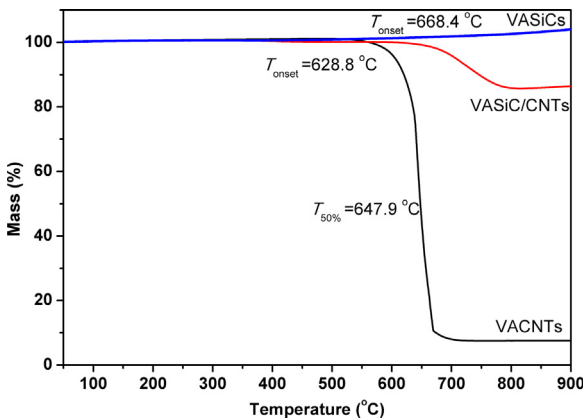


**Fig. 6.** TGA profiles of VACNTs, VASiC/CNTs and VASiCs in air (80 sccm) indicating the presence of catalyst residues (5.2 wt%) in VACNTs, the partial conversion of CNT-SiC in VASiC/CNTs (15.4 wt% CNTs unconverted) and the surface oxidation of VASiCs between 600 and 900 °C (2.8 wt% gained mass).

appeared in both VASiC/CNTs and VASiCs. They are 35.7°, 41.4°, 60.1°, 71.8° and 75.6°, corresponding to the (111), (200), (220), (311) and (222) lattice planes of cubic SiC ( $\beta$ -SiC), respectively (JCPDS #02-1050). The small peak at 33.6° is due to stacking faults which is quite common for SiC [54]. Residues of CNTs and SiO<sub>2</sub> (peak at 22°, JCPDS #03-0271) were also present in the VASiC/CNTs sam-

ple. Calcination in air and NaOH treatment of the VASiC/CNTs and the VASiCs samples removed the CNTs and SiO<sub>2</sub> and the catalyst residues respectively (Fig. 4b).

The Raman spectra (Fig. 5) show a typical D band (1341 cm<sup>-1</sup>), G band (1574 cm<sup>-1</sup>) and G' band (2684 cm<sup>-1</sup>) of multi-wall CNTs for the VACNTs sample. The intensity ratio of D band and G band ( $I_{D/G}$ ) is 0.33, indicating the low defect intensity of MWCNT [37]. For the VASiC/CNTs, two peaks are present at 794 cm<sup>-1</sup> and 967 cm<sup>-1</sup> and they are attributed to the transverse optical (TO) mode and the longitudinal optical (LO) mode of cubic SiC [55]. Whilst the VACNT residue was only 14.3 wt%, its Raman intensity was significantly higher than that of VASiCs. Although no obvious CNT peaks could be found in the VASiCs XRD patterns, Raman peaks of CNT could still be observed due to the much stronger Raman intensity of CNT, even traces of which will contribute to significant Raman peaks. The reason that trace of CNT is always present even after calcination in Air could be possible encapsulation of CNT (a very small portion) by the formed SiC. In addition, there are two small Raman peaks at 1510 cm<sup>-1</sup> and 1694 cm<sup>-1</sup> for the VASiCs indicating the formation of S-C bonds [56].

To investigate the thermal stability of samples, TGA was carried out in air up to 900 °C. The temperature at 50% mass loss for VACNTs is 647.9 °C (Fig. 6), which is among the highest in CNTs from different precursors and synthesis conditions (574 – 649 °C) [37,47]. There is still 7.4 wt% residue at 900 °C, corresponding to 5.2 wt% of iron-based catalyst assuming that all catalyst is converted to Fe<sub>2</sub>O<sub>3</sub>. TGA profile shows that 14.3 wt% mass loss was observed for

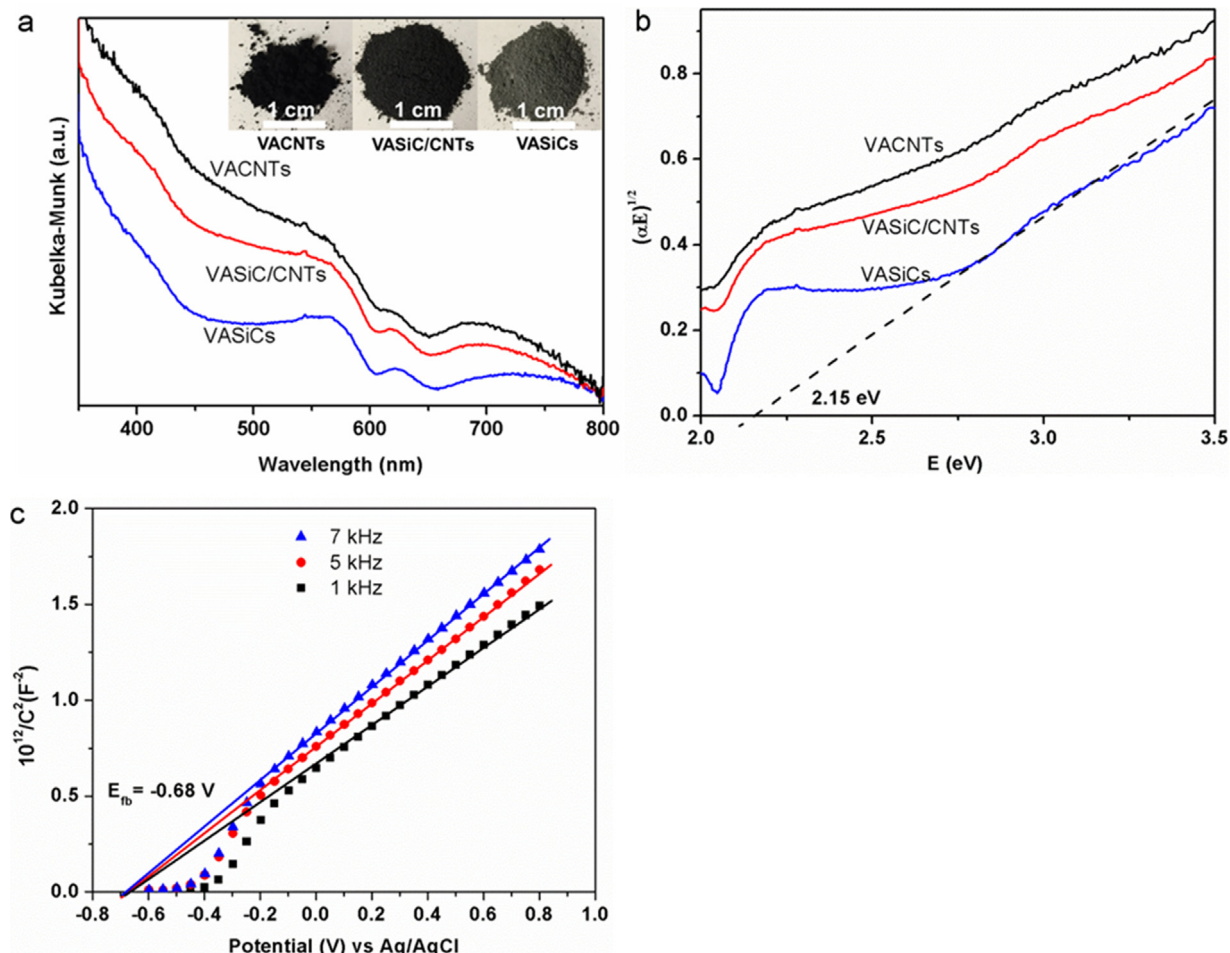


**Fig. 7.** (a) UV-vis DRS of VACNTs, VASiC/CNTs and VASiCs with photos of samples after grinding into powder (inset) showing the grey colour of VASiCs and their light absorbance edge of 577 nm; (b) Indirect band gap estimation (2.15 eV) for VASiCs from the plotting of  $(\alpha E)^{1/2}$  versus photon energy (eV); (c) Mott-Schottky plots of VASiCs in Na<sub>2</sub>SO<sub>4</sub> aqueous solution (0.2 M) showing the flat band potential ( $E_{fb}$ ) of −0.68 V.

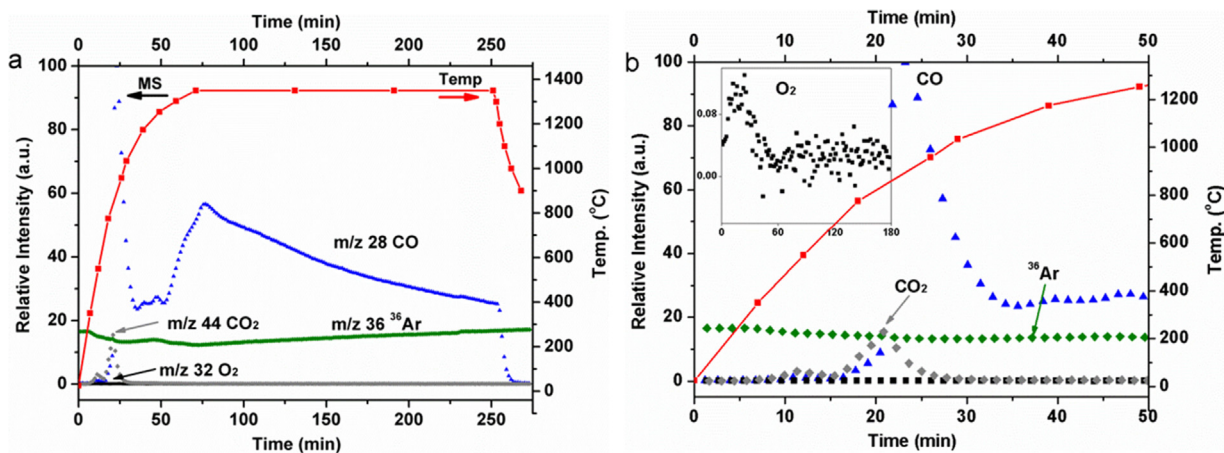


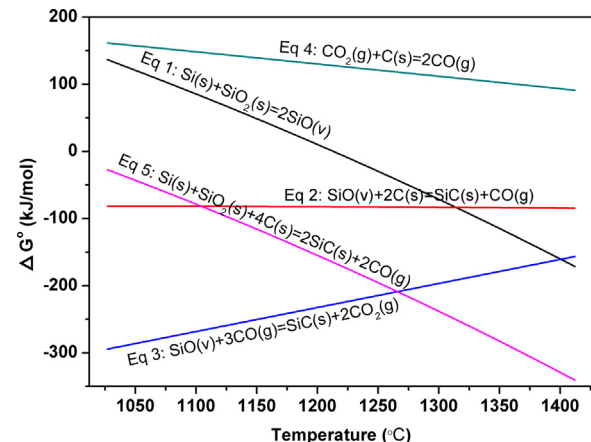
**Fig. 8.** (a) Real-time monitoring of the gas residuals from the VASiCs synthesis: profiles of  $m/z$  28,  $m/z$  32,  $m/z$  36,  $m/z$  44 (left y-axis) and furnace temperature (right y-axis) versus the reaction time showing the generation of CO as the only by-product, starting at  $1150\text{ }^{\circ}\text{C}$  and reaching maximum at  $1350\text{ }^{\circ}\text{C}$ . (b) Close-up view of graph B in the time range of 0–50 min showing the stability of  $^{36}\text{Ar}$ , low level of  $\text{O}_2$  and the generation of CO and  $\text{CO}_2$  at lower temperature from the oxidation of CNTs or organic residues.

VASiC/CNTs, from which the mass ratio of un-converted CNTs in VASiC/CNTs can be calculated to be 15.4 wt%. In addition, the onset temperature increased from  $628.8\text{ }^{\circ}\text{C}$  for VACNTs to  $668.4\text{ }^{\circ}\text{C}$  for VASiC/CNTs, demonstrating the enhanced thermal stability of CNTs in VASiC/CNTs. This could be attributed to the interaction between SiC and CNT [20]. VASiCs after CNTs removal is thermally stable with only 2.8 wt% gained mass between  $600\text{ }^{\circ}\text{C}$  and  $900\text{ }^{\circ}\text{C}$  due to the oxidation of exposed surface of SiC nanowires [57].

Furthermore, UV-vis DRS was used to evaluate the light absorbance capacity of the samples. The VACNTs have the strongest light absorbance (Fig. 7a), as indicated by its strong dark colour (Fig. 7a inset). The VASiC/CNTs has a medium light absorbance between VASiCs and VACNTs. VASiCs are in grey colour, which is lighter than the others. However, it still has strong light absorbance in the UV range and is visible light responsive up to 577 nm (the absorbance edge). SiC is well known to possess an indirect band gap. Extrapolating from the plot of  $(\alpha h\nu)^{1/2}$  versus photon energy (eV) (Fig. 7b) gave an estimated band gap of VASiCs as 2.15 eV, which indicated its potential as visible-light-driven photocatalyst. The estimated band gap is slightly narrower than the reported value (2.2 eV) for cubic SiC nanowires [46], which could be due to the presence of trace carbon in VASiCs that cannot be completely removed during the synthesis. From Mott-Schottky measurement (Fig. 7c), the conduction band of VASiCs was estimated to be  $-0.68\text{ eV}$ . By combining the band gap of 2.15 eV, the valence band of VASiCs can be given (1.47 eV).

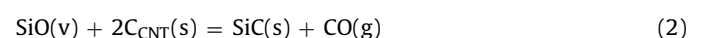
### 3.2. Growth mechanism of VASiCs

In order to study the growth mechanism of VASiCs, the abundance of analytes at  $m/z = 28, 32, 36, 40$  and  $44$  as well as furnace temperature during the synthesis were monitored. The relative abundance of  $^{36}\text{Ar}$  remains relatively constant at around 15% (Fig. 8a). This suggests that: a) the flow of the carrier gas in the reactor is stable; and b) any change in the abundance of existing analytes or evolution of any new analytes could be attributed to the carbothermic reaction but not from the fluctuation of the carrier gas diluting or concentrating the analytes. The  $m/z$  32 ( $\text{O}_2$ ) (Fig. 8) is at a very low level ( $10^{-11}$  torr) ruling out any air leakage in the system. Therefore, the fragment at  $m/z$  28 can be exclusively assigned to CO while the  $m/z$  44 can be assigned to  $\text{CO}_2$ . During the heating-up cycle of the CVD experiment, two peaks for CO and  $\text{CO}_2$  appeared at  $550\text{ }^{\circ}\text{C}$  and  $800\text{ }^{\circ}\text{C}$ , respectively. These peaks may originate from the oxidation of CNTs or organic residues introduced during the  $\text{SiO}_2$  infiltration. At  $1150\text{ }^{\circ}\text{C}$ ,  $\text{SiO}$  started to form Eq. (1)



**Fig. 9.** Gibbs free energy of change ( $\Delta G^{\circ}$ ) versus temperature ( $1027\text{--}1412\text{ }^{\circ}\text{C}$ ) for the etching of MWCNTs (Eqs. (1)–(5) showing the reaction in ding to the etching of MWCNTs (Eq. (1)) becomes spontaneous at  $1210\text{ }^{\circ}\text{C}$  while the reactions in ding to the etching of MWCNTs (Eq. (2) and (3) are spontaneous and the reaction in ding to the etching of MWCNTs (Eq. (4)) is non-spontaneous in the investigated temperature.

and then reacted with VACNTs to produce VASiCs and CO as a by-product (Eq. (2)) [40,42]. Hence, the profile of CO generation could be correlated with the formation of SiC. The slow increase of  $m/z$  28 between  $1150\text{ }^{\circ}\text{C}$  –  $1250\text{ }^{\circ}\text{C}$  (30–50 mins) showed the gradual generation of CO initially, followed by a sharp increase (50–75 mins), reaching a maximum at  $1350\text{ }^{\circ}\text{C}$  (75 mins) implying a similar trend for the VASiCs formation. The CO intensity decreased slowly and returned to a level similar to that at  $1150\text{ }^{\circ}\text{C}$  indicating the end of the VACNTs to VASiCs conversion. It was reported that SiC can also form through the reaction of  $\text{SiO}$  with CO (Eq. (3)) releasing  $\text{CO}_2$  as a by-product [40,42]. It was speculated that  $\text{CO}_2$  partly etches the CNTs (Eq. (4)) leading to shorter and thinner SiC nanowires when compared to their CNT templates [40,42]. However, no  $\text{CO}_2$  peak could be observed in the mass spectra (MS) (Fig. 8) at temperatures above  $1150\text{ }^{\circ}\text{C}$  suggesting that the formation of the VASiCs through the reaction described by Eq. (3) is less likely. In addition, there was no obvious  $\text{CO}_2$  etching effect observed on the obtained VASiCs in our work and the carpet height of VASiC (ca. 1 mm) was very close to that of the CNT template.



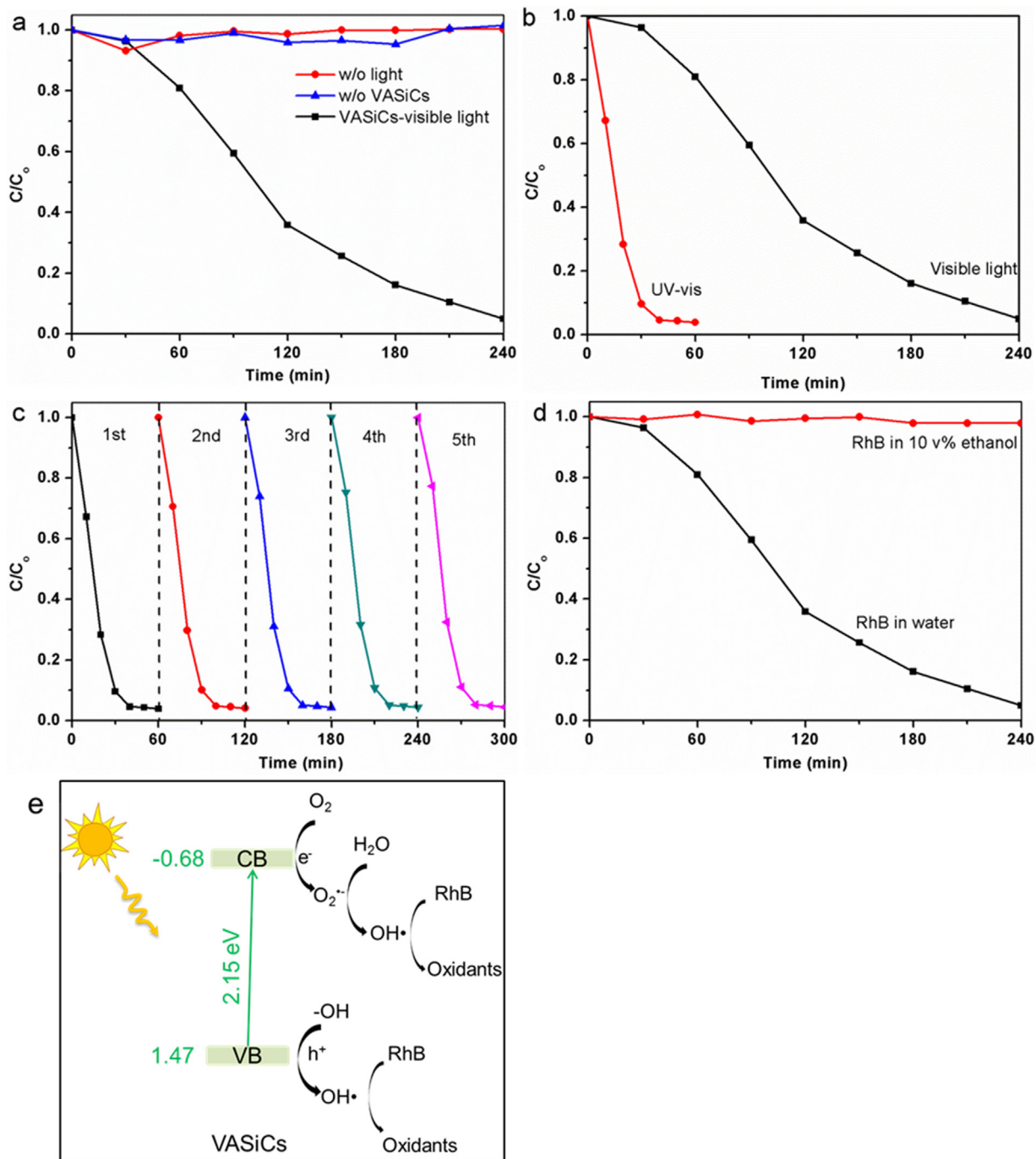
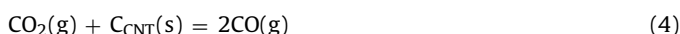
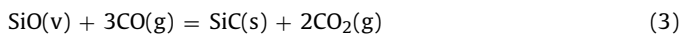


**Fig. 10.** Photocatalytic RhB degradation (a) under control conditions showing no removal of RhB without light or VASiCs and (b) with different light source showing >90% RhB removal within 30 min (UV-vis) and >95% RhB removal within 4 h (Visible light). Conditions: 10 mg VASiCs in 50 ml RhB (10 mg l<sup>-1</sup>); light source: 300 W Xe lamp, visible light: 400–800 nm, UV-vis: 260–800 nm. (c) Recycle studies showing the good recyclability of VASiCs. (d) Control studies of the RhB degradation pathway by quenching the hydroxyl radical (OH<sup>•</sup>) with ethanol revealing RhB degradation through OH<sup>•</sup>. (e) Proposed RhB degradation mechanism demonstrating that both photo-excited electrons (e<sup>-</sup>) and holes (h<sup>+</sup>) can be used to generate hydroxyl radical (OH<sup>•</sup>) for the removal of RhB.



The Gibbs free energy of change ( $\Delta G^\circ$ ) for possible reactions (Eqs. (1)–(5)) involved in the SiC formation was calculated using thermochemistry data [58] and plotted versus temperature (Fig. 9). In theory, the reaction described by Eq. (1) should be spontaneous ( $\Delta G^\circ < 0$ ) above 1210 °C. In this temperature range, SiO always

reacts spontaneously with C to form SiC (Eq. (2)). *In situ* mass spectrometry revealed a sudden increase of CO (see Eq. (2) and Fig. 8) at a slightly higher temperature, e.g. 1245 °C indicating the formation of SiO following Eq. (1) and SiC according to Eq. (2). As discussed above, no peak for CO<sub>2</sub> from Eq. (3) was observed in MS despite of the negative  $\Delta G^\circ$  for this reaction. Moreover, no CO<sub>2</sub> etching of MWCNTs can be found by the SEM/TEM. In fact, the reaction corresponding to the etching of MWCNTs (Eq. (4)) is non-spontaneous. Based on the *in situ* MS studies, *ex situ* characterisation and thermodynamic analysis, the growth of VASiCs was illustrated to be via the

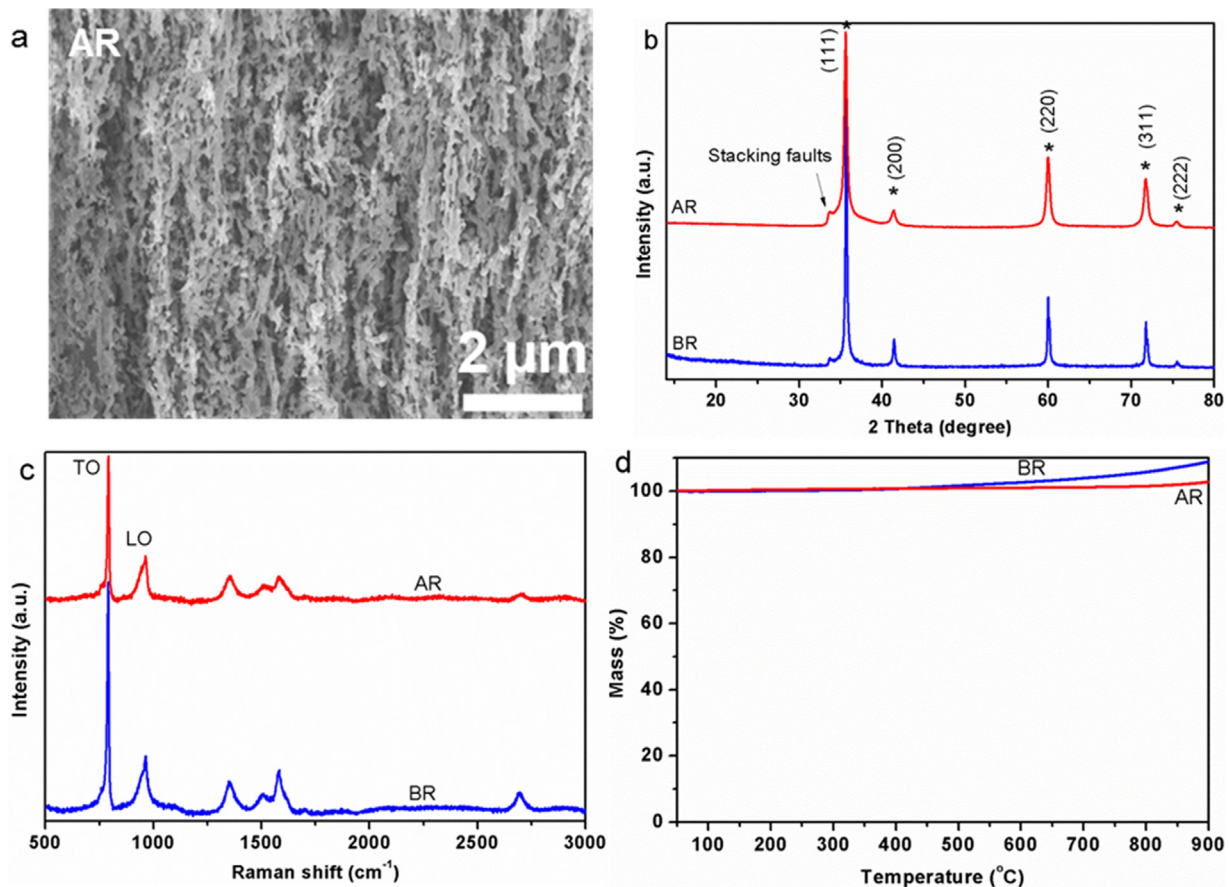


**Fig. 11.** Characterisation of VASiCs before (BR) and after (AR) photoreaction: (a) SEM image, (b) XRD patterns, and (c) Raman spectra showing the maintenance of morphology and crystal structure in VASiCs after photo-reaction, and (d) TGA profiles revealing the reduction of exposed surface in VASiCs after photo-reaction.

reactions in Eqs. (1) and (2), the total reaction of which was showed in Eq. (5). Theoretically, 1410 mg of VASiCs per 1000 mg VACNTs should be produced based on ding to the etching of MWCNTs (Eq. (5)) and 84.6 wt% of CNT-SiC conversion (calculated from TGA data). Typically, 1280 mg VASiCs per 1000 mg VACNTs template could be collected experimentally which is close to the theoretical value. These results further prove that the formation of VASiCs follows the reactions in ding to the etching of MWCNTs (Eq. (1)) and ding to the etching of MWCNTs (Eq. (2)).

### 3.3. Photocatalytic degradation studies of RhB

Until today, only photocatalytic performance under UV light has been reported for aligned SiC nanowires [14]. VASiCs are estimated to have a band gap of 2.15 eV, hence they are likely to harvest and utilise the visible light. In order to illustrate this, both UV-vis and visible light were used to evaluate the VASiCs for the photocatalytic degradation of RhB. The Relative Standard Deviation for the photocatalytic tests was 4.4%. The control studies in Fig. 10a show that there is no obvious RhB degradation either in the dark or without VASiCs while RhB can be efficiently removed with both VASiCs and light irradiation. These results confirmed that the removal of RhB was from the photocatalytic reaction. The results in Fig. 10b show that VASiCs are very effective in decomposing the RhB using UV-vis, with more than 90% RhB degraded within 30 mins. After adding the cut-off filter to remove UV light, 95% RhB removal can be achieved within 4 h, proving that the VASiCs are indeed visible-light-responsive. Recycle studies (Fig. 10c) showed that VASiCs can be recycled for at least five runs with slightly loss of photo-activity. In order to illustrate the RhB degradation pathway, ethanol (10 v%)

was added in the RhB solution to quench the hydroxyl radical ( $\text{OH}^\bullet$ ). Since no RhB was removed after adding ethanol, we concluded that the RhB was entirely oxidised and degraded by  $\text{OH}^\bullet$  while the oxidation by hole can be neglected here (Fig. 10d) [59]. A possible RhB degradation pathway could be as follows: Under light irradiation, electrons were excited from the valence band to the conduction band of the VASiCs when the photon energy is higher than their band gap. The photo-generated electrons ( $e^-$ ) then reacted with dissolved molecular oxygen to form superoxide radicals ( $\text{O}_2^{\bullet-}$ ) which can be further converted to  $\text{OH}^\bullet$  [60]. Meanwhile,  $\text{OH}^\bullet$  can also be produced from the oxidation of hydroxyl group ( $-\text{OH}$ ) by the photo-generated hole ( $\text{h}^+$ ) [60]. These as-generated  $\text{OH}^\bullet$  are highly oxidising radicals which contributed to the degradation of RhB.

To study the stability of VASiCs under light irradiation, VASiCs were collected and characterised by SEM, XRD, Raman and TGA after photo-reaction. SEM and XRD studies (Fig. 11) showed that both morphology and crystal structure of the VASiCs were mostly maintained after photo-reaction. However, TGA profiles revealed that the exposed VASiCs surface was reduced after photo-reaction evidenced by the reduced mass gain of the sample. As a result, we have developed vertically-aligned SiC nanowires with tunable structure, which showed visible-light-driven photocatalytic activity with good recyclability and stability.

## 4. Conclusions

We reported a method to produce vertically aligned SiC nanowires in gram scale using aligned CNTs template. The as obtained VASiCs have vertically aligned orientation and maintain the structure of the CNTs template hence allowing the control of

their structure. The *in situ* monitoring of gas residuals and *ex situ* characterisation of the produced materials revealed that VASiCs were generated from the reaction of SiO with CNTs at a temperature range of 1150–1350 °C. CO was found to be the only by-product, whilst CO<sub>2</sub> was not detected in this study. Furthermore, the VASiCs are crystalline with a cubic crystal structure, showing strong light absorbance in the UV-vis range up to 577 nm and have estimated band gap of 2.15 eV. Photocatalytic evaluation showed that the VASiCs can decompose 90% RhB within 30 min under UV-vis or more than 95% RhB within 4 h under visible light without adding any cocatalyst. Besides, VASiCs showed good stability and can be recycled for at least five times without significant loss of photoactivity. We believe these findings will contribute to the design of aligned SiC nanowires for other energy and environmental applications.

## Acknowledgements

This project has received funding from the European Union's Horizon 2020 research and innovation programme under the Marie Skłodowska-Curie grant agreement No 654723. The authors are also grateful for the financial support received from European Commission's 7th Framework Program FP7-PEOPLE-ITN-2008-238363 CONTACT), the European Research Council (ERC-2009-StG-240500 DEDIGROWTH; ERC-2012-PoC-309786 DEVICE; ERC-2015-PoC-680559 CONDUCT), The Royal Society, EPSRC fellowship program (DTA), Pathways to Impact grants, and Impact Acceleration Accounts, and the ERDC for their financial support.

## Appendix A. Supplementary data

Supplementary data associated with this article can be found, in the online version, at <http://dx.doi.org/10.1016/j.apcatb.2017.06.056>.

## References

- [1] N.S. Lewis, D.G. Nocera, Proc. Natl. Acad. Sci. USA 103 (2006) 15729–15735.
- [2] A. Kudo, Y. Miseki, Chem. Soc. Rev. 38 (2009) 253–278.
- [3] H. Tong, S. Ouyang, Y. Bi, N. Umezawa, M. Oshikiri, J. Ye, Adv. Mater. 24 (2012) 229–251.
- [4] K. Evanoff, J. Khan, A.A. Balandin, A. Magasinski, W.J. Ready, T.F. Fuller, G. Yushin, Adv. Mater. 24 (2012) 533–537.
- [5] S. Li, Y. Luo, W. Lv, W. Yu, S. Wu, P. Hou, Q. Yang, Q. Meng, C. Liu, H.M. Cheng, Adv. Energy Mater. 1 (2011) 486–490.
- [6] Y. Xu, M. Zhou, L. Wen, C. Wang, H. Zhao, Y. Mi, L. Liang, Q. Fu, M. Wu, Y. Lei, Chem. Mater. 27 (2015) 4274–4280.
- [7] H. Zhang, G. Cao, Z. Wang, Y. Yang, Z. Shi, Z. Gu, Nano Lett. 8 (2008) 2664–2668.
- [8] X. Lu, G. Wang, T. Zhai, M. Yu, J. Gan, Y. Tong, Y. Li, Nano Lett. 12 (2012) 1690–1696.
- [9] T. Krishnamoorthy, V. Thavasi, S. Ramakrishna, Energy Environ. Sci. 4 (2011) 2807–2812.
- [10] J.H. Park, S. Kim, A.J. Bard, Nano Lett. 6 (2006) 24–28.
- [11] G. Wang, H. Wang, Y. Ling, Y. Tang, X. Yang, R.C. Fitzmorris, C. Wang, J.Z. Zhang, Y. Li, Nano Lett. 11 (2011) 3026–3033.
- [12] W.M. Zhou, L.J. Yan, Y. Wang, Y.M. Zhang, Appl. Phys. Lett. 89 (2006) 1–3.
- [13] J.-Y. Hao, Y.-Y. Wang, X.-L. Tong, G.-Q. Jin, X.-Y. Guo, Int. J. Hydrogen Energy 37 (2012) 15038–15044.
- [14] H. Liu, G. She, L. Mu, W. Shi, Mater. Res. Bull. 47 (2012) 917–920.
- [15] Y. Wang, X. Guo, L. Dong, G. Jin, Y. Wang, X.-Y. Guo, Int. J. Hydrogen Energy 38 (2013) 12733–12738.
- [16] O. Haibo, H. Jianfeng, Z. Xierong, C. Liyun, L. Cuiyan, X. Xinbo, F. Jie, Ceram. Int. 40 (2014) 2619–2625.
- [17] Y. Zhang, T. Xia, P. Wallenmeyer, C.X. Harris, A.A. Peterson, G.A. Corsiglia, J. Murowchick, X. Chen, Energy Technol. 2 (2014) 183–187.
- [18] M. Wang, J. Chen, X. Liao, Z. Liu, J. Zhang, L. Gao, Y. Li, Int. J. Hydrogen Energy 39 (2014) 14581–14587.
- [19] J. Zhang, J. Chen, L. Xin, M. Wang, Mater. Sci. Eng. B 179 (2014) 6–11.
- [20] X. Zhou, X. Li, Q. Gao, J. Yuan, J. Wen, Y. Fang, W. Liu, S. Zhang, Y. Liu, Catal. Sci. Technol. 5 (2015) 2798–2806.
- [21] Y. Wang, L. Zhang, X. Zhang, Z. Zhang, Y. Tong, F. Li, J.C.S. Wu, X. Wang, Appl. Catal. B: Environ. 206 (2017) 158–167.
- [22] B. Wang, Y. Wang, Y. Lei, N. Wu, Y. Gou, C. Han, S. Xie, D. Fang, Nano Res. (2015) 1–13.
- [23] Z.W. Pan, H.L. Lai, F.C.K. Au, X.F. Duan, W.Y. Zhou, W.S. Shi, N. Wang, C.S. Lee, N.B. Wong, S.T. Lee, S.S. Xie, Adv. Mater. 12 (2000) 1186–1189.
- [24] G. Xi, Y. Liu, X. Liu, X. Wang, Y. Qian, J. Phys. Chem. B 110 (2006) 14172–14178.
- [25] H. Wang, L. Lin, W. Yang, Z. Xie, L. An, J. Phys. Chem. C 114 (2010) 2591–2594.
- [26] L. Wang, C. Li, Y. Yang, S. Chen, F. Gao, G. Wei, W. Yang, ACS Appl. Mater. Interfaces 7 (2014) 526–533.
- [27] A. Khan, C. Jacob, Mater. Lett. 135 (2014) 103–106.
- [28] H.Y. Kim, J. Park, H. Yang, Chem. Commun. (2003) 256–257.
- [29] Z. Li, J. Zhang, A. Meng, J. Guo, J. Phys. Chem. B 110 (2006) 22382–22386.
- [30] R. Wu, K. Zhou, X. Qian, J. Wei, Y. Tao, C.H. Sow, L. Wang, Y. Huang, Mater. Lett. 91 (2013) 220–223.
- [31] S. Xu, G. Qiao, H. Wang, D. Li, T. Lu, Mater. Lett. 62 (2008) 4549–4551.
- [32] J.J. Niu, J.N. Wang, J. Phys. Chem. B 111 (2007) 4368–4373.
- [33] J.J. Niu, J.N. Wang, Q.F. Xu, Langmuir 24 (2008) 6918–6923.
- [34] Y. Yang, G. Meng, X. Liu, L. Zhang, Z. Hu, C. He, Y. Hu, J. Phys. Chem. C 112 (2008) 20126–20130.
- [35] Z. Pan, S. Xie, B. Chang, L. Sun, W. Zhou, G. Wang, Chem. Phys. Lett. 299 (1999) 97–102.
- [36] S.S. Meysami, F. Dillon, A.A. Koós, Z. Aslam, N. Grobert, Carbon 58 (2013) 151–158.
- [37] S.S. Meysami, A.A. Koós, F. Dillon, M. Dutta, N. Grobert, Carbon 88 (2015) 148–156.
- [38] G. Otieno, Processing and Properties of Aligned Carbon Nanotube/glass Ceramic Composite, Oxford University, 2012.
- [39] G. Otieno, A.A. Koós, F. Dillon, A. Wallwork, N. Grobert, R.I. Todd, Carbon 48 (2010) 2212–2217.
- [40] W.Q. Han, S.S. Fan, Q.Q. Li, W.J. Liang, B.L. Gu, Chem. Phys. Lett. 265 (1997) 374–378.
- [41] C.C. Tang, S.S. Fan, H.Y. Dang, J.H. Zhao, C. Zhang, P. Li, Q. Gu, J. Cryst. Growth 210 (2000) 595–599.
- [42] S.C. Chiu, Y.Y. Li, J. Cryst. Growth 311 (2009) 1036–1041.
- [43] M. Paulose, K. Shankar, O.K. Varghese, G.K. Mor, C.A. Grimes, J. Phys. D: Appl. Phys. 39 (2006) 2498.
- [44] Y.J. Hwang, C. Hahn, B. Liu, P. Yang, ACS Nano 6 (2012) 5060–5069.
- [45] R. Mohan, K. Krishnamoorthy, S.-J. Kim, Chem. Phys. Lett. 539 (2012) 83–88.
- [46] G. Attolini, F. Rossi, F. Fabbri, M. Bosi, G. Salviati, B.E. Watts, Nanowires, InTech, 2010.
- [47] S.S. Meysami, A.A. Koós, F. Dillon, N. Grobert, Carbon 58 (2013) 159–169.
- [48] Y.-J. Hao, J.B. Wagner, D.S. Su, G.-Q. Jin, X.-Y. Guo, Nanotechnology 17 (2006) 2870.
- [49] D.-H. Wang, D. Xu, Q. Wang, Y.-J. Hao, G.-Q. Jin, X.-Y. Guo, K. Tu, Nanotechnology 19 (2009) 215602.
- [50] J. Wei, K.-Z. Li, H.-J. Li, Q.-G. Fu, L. Zhang, Mater. Chem. Phys. 95 (2006) 140–144.
- [51] G.-Y. Li, X.-D. Li, H. Wang, L. Liu, Solid State Sci. 11 (2009) 2167–2172.
- [52] R. Andrews, D. Jacques, D. Qian, E. Dickey, Carbon 39 (2001) 1681–1687.
- [53] S.S. Meysami, P. Dallas, J. Britton, J.G. Lozano, A.T. Murdock, C. Ferraro, E.S. Gutierrez, N. Rijnveld, P. Holdway, K. Porfyrikis, Nanoscale 8 (2016) 11993–12001.
- [54] V.V. Pujar, J.D. Cawley, J. Am. Ceram. Soc. 78 (1995) 774–782.
- [55] M. Bechelany, A. Brioude, D. Cornu, G. Ferro, P. Miele, Adv. Funct. Mater. 17 (2007) 939–943.
- [56] Y. You, T. Yu, J. Kasim, H. Song, X. Fan, Z. Ni, L. Cao, H. Jiang, D. Shen, J. Kuo, Appl. Phys. Lett. 93 (2008) 103111.
- [57] J. Prakash, K. Dasgupta, B. Kumar, S.K. Ghosh, J. Chakravarthy, Surf. Coat. Technol. 259 (2014) 637–646.
- [58] M.W. Chase, J. Phys. Chem. Ref. Data 25 (1996) 551–603.
- [59] J. Hong, C. Chen, F.E. Bedoya, G.H. Kelsall, D. O'Hare, C. Petit, Catal. Sci. Technol. 6 (2016) 5042–5051.
- [60] N. Daneshvar, D. Salari, A. Khataee, J. Photochem. Photobiol. A 162 (2004) 317–322.